JAAS

Cite this: *J. Anal. At. Spectrom.*, 2012, **27**, 1101

www.rsc.org/jaas

PAPER

Measurement of elemental concentration of aerosols using spark emission spectroscopy†

Prasoon K. Diwakar and Pramod Kulkarni*

Received 31st January 2012, Accepted 30th March 2012
DOI: 10.1039/c2ja30025g

A coaxial microelectrode system has been used to collect and analyse the elemental composition of aerosol particles in near real-time using spark emission spectroscopy. The technique involves focused electrostatic deposition of charged aerosol particles onto the flat tip of a microelectrode, followed by introduction of spark discharge. A pulsed spark discharge was generated across the electrodes with input energy ranging from 50 to 300 mJ per pulse, resulting in the formation of controlled pulsed plasma. The particulate matter on the cathode tip is ablated and atomized by the spark plasma, resulting in atomic emissions which are subsequently recorded using a broadband optical spectrometer for element identification and quantification. The plasma characteristics were found to be very consistent and reproducible even after several thousands of spark discharges using the same electrode system. The spark plasma was characterized by measuring the excitation temperature (~7000 to 10 000 K), electron density (~10^{16} cm^{-3}), and evolution of spectral responses as a function of time. The system was calibrated using particles containing Pb, Si, Na and Cr. Absolute mass detection limits in the range 11 pg to 1.75 ng were obtained. Repeatability of spectral measurements varied from 2 to 15%. The technique offers key advantages over similar microplasma-based techniques such as laser-induced breakdown spectroscopy, as: (i) it does not require any laser beam optics and eliminates any need for beam alignment, (ii) pulse energy from dc power supply in SIBS system can be much higher compared to that from laser source of the same physical size, and (iii) it is quite conducive to compact, field-portable instrumentation.

Introduction

Exposure to airborne particles containing toxic metals from industrial activities such as mining, welding, cutting, brazing, and soldering pose a significant health risk in industrial and ambient environments.[1–6] The emergence of nanotechnology has also raised many concerns about potential health risks from the inhalation of engineered nanoparticles, prompting the need for reliable measurement tools with very low detection limits.[7] Existing methods for the measurement of particulate chemical composition involve filter-based collection over several hours, followed by laboratory analysis of collected particulate matter using suitable analytical methods. These off-line methods are prone to large errors introduced by sampling artefacts as well as operator bias, and do not provide instantaneous information about aerosol composition which is valuable in many applications. As a result, there is a growing interest in developing field-portable, near-real-time instruments that can measure multielemental composition to facilitate effective exposure measurement and hazard identification.[8]

To address the above need, we have recently developed an aerosol preconcentration method that allows efficient coupling of aerosol sampling with emission spectroscopy.[9] By using this preconcentration technique with laser-induced breakdown spectroscopy (LIBS), we have shown that excellent accuracy, precision, limits of detection, and sampling statistics can be achieved.[9] Furthermore, the technique is readily amenable to miniaturization (necessary in field-portable instrumentation), and also allows near real-time measurement capability with a time resolution of a few seconds to a few minutes. In this study, we extend this preconcentration method to spark emission spectroscopy to demonstrate its superior potential as a candidate for making aerosol measurements at low detection limits, and with good accuracy and precision. Our aerosol preconcentration method involves collection of airborne particles on the tip of a microelectrode, a few hundred micrometres in diameter, using electrostatic forces. The coaxial microelectrode system, originally designed for aerosol preconcentration, is also inherently suited

Center for Disease Control and Prevention, National Institute for Occupational Safety and Health, 4676 Columbia Parkway, MS R7, Cincinnati, OH, 45226, USA. E-mail: Pskulkarni@cdc.gov

† *Disclaimer*: the findings and conclusions in this report are those of the authors and do not necessarily represent the views of the National Institute for Occupational Safety and Health. Mention of product or company name does not constitute endorsement by the Centers for Disease Control and Prevention.

for spark generation for analyte excitation. In addition, the other advantages of spark emission spectroscopy include: (i) considerable simplicity due to lack of laser beam shaping optics and alignment, (ii) ability to obtain high energy per pulse relative to a laser source of the same physical size, and (iii) the compact size of spark generation and spectroscopic hardware making it ideal for field-portable instrumentation.

Traditional spark emission spectroscopy has existed for more than a century and has been studied and used as an analytical source of excitation for elemental detection.[10–12] Walters and coworkers have published extensive reviews on this topic.[11–22] In typical spark emission spectroscopy, electric discharge between the electrodes leads to plasma formation and subsequent ablation of analyte sample from the electrode, which is typically a cathode. Ablated material is vaporized, atomized and electronically excited in the plasma. Typical detection limits for the analysis of solids using spark emission spectroscopy range from a few ppm to a few 100 ppb; in terms of absolute mass, sub-nanogram detection limits have been reported.[23–26] Spark spectroscopy has also been applied to analysis of airborne particles with limited success. Hunter *et al.* used an electrode system to create spark plasma in the inter-electrode space where the aerosol sample passed through, which allowed on-the-fly emission detection and quantification, albeit with poor limits of detection (in the range 10–1200 μg m^{-3}) and sampling statistics.[27,28]

In this study we use our aerosol preconcentration method with spark emission spectroscopy to demonstrate that multielemental measurements can be made with excellent figures of merit. We show that limits of detection, as low as a few ng m^{-3} can be achieved using our system.

Experimental section

Materials and methods

The experimental setup is similar to that described in our previous study and is shown in Fig. 1.[9] A list of key components of the experimental setup is provided in Table 1. The experimental setup consists of four components: (i) aerosol generation, (ii) aerosol collection system, (iii) pulsed spark generation hardware, and (iv) the optical detection system. Test aerosol was generated using a pneumatic atomizer (Model 3080, TSI Inc., Shoreview, MN) which was then passed through two sequential diffusion dryers for desolvating the droplets. The dry aerosol was introduced in the differential mobility analyser (DMA) to obtain near-monodisperse test aerosols of desired size (with geometric standard deviation less than 1.1). In this study, particles of 150 nm diameter were used for all the measurements. The resulting positively charged near-monodisperse test aerosol from the DMA was then sent to the aerosol preconcentration or collection unit for analysis using spark emission spectroscopy. A constant flow rate of 1.5 l min^{-1} was maintained through the aerosol collection system and was driven by the native pump in the condensation particle counter (CPC). The near-monodisperse charged particles were then introduced into an electrostatic aerosol collection unit (described below), where they quickly migrated to the tip of a grounded electrode under the influence of an external electrical field. Once a predetermined amount of particulate mass was collected on the electrode tip, high voltage pulse was applied to generate a spark discharge across the ground electrode and an opposing, coaxial high-voltage electrode. This pulse spark led to vaporization and atomization of the particulate mass; the ensuing atomic emission was detected and analyzed by a broadband spectrometer.

An electrostatic aerosol collection system designed in an earlier study was used;[9] the same system was also used for spark plasma generation. As shown in Fig. 2, this system consists of two coaxial electrodes with their tips separated by a few millimetres. The coaxial electrode system is used to create an external electrical field such that the charged particles can preferentially migrate to the tip of the ground electrode. The electrode system is also used to apply a high voltage pulse to create spark plasma for spectroscopic analysis of the particles deposited on the electrode. A 500 μm diameter, flat-tip tungsten needle which served as

Table 1 Key components of the experimental setup

HV pulse generator	Vtech Engineering Corp.
Spectrometer	LIBS 2500 plus, Ocean Optics
HV power supply for aerosol collection	Bertran S-230, Spellman HV
Condensation particle counter	Model 3022A, TSI Inc.
Differential mobility analyzer	Model 3080, TSI Inc.
Pneumatic atomizer	Model 3076, TSI Inc.
Digital delay generator	Model 9600, Quantum Composers
Quartz window and lenses	CVI Melles Griot
Chemical standards	Spex Certiprep, Fisher Scientific, Inorganic Ventures

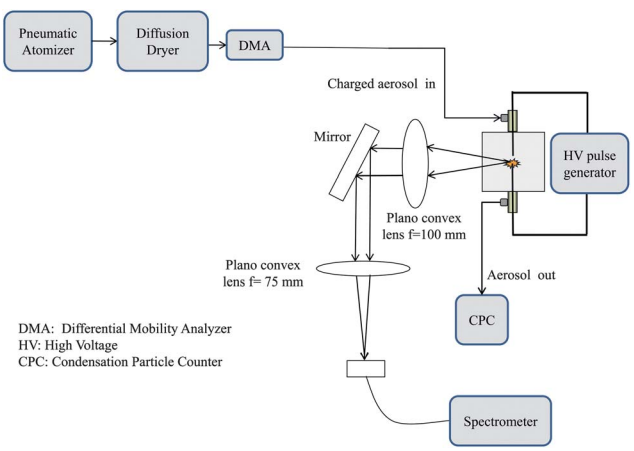

Fig. 1 Schematic diagram of the experimental setup.

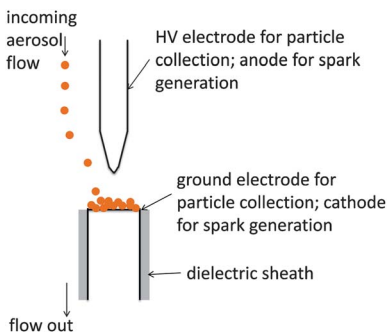

Fig. 2 The spark electrode setup.

a ground electrode, was used for aerosol preconcentration. The walls of the ground electrode were insulated with dielectric material, with the flat tip exposed, to avoid particle deposition on the electrode walls. The opposing, coaxial high voltage electrode consisted of a 200 μm tungsten needle with a sharp tip of about 5 μm diameter. A positive potential (~3 kV) was applied to the high voltage electrode to create an intense electric field at its tip for the purpose of particle collection. Both the electrodes were coaxially aligned, with a distance of 5 mm between the tip of the high voltage electrode and the flat surface of the collection electrode. Positively charged particles from the DMA entered the collection system through a concentric tube around the high voltage electrode. The electric field between the high voltage electrode and the collection electrode (grounded) led to the migration of charged particles to the tip of the collection electrode.

The collection electrode also served as the cathode while the high voltage electrode served as the anode for the spark generation. The dc potential on the high voltage electrode—needed to create an external field for particle collection—was turned off during the application of the pulsed voltage for spark generation. The aerosol sample flow of 1.5 l min^{-1} exited the collection system through a concentric tube around the collection electrode. A CPC was used downstream of the aerosol collection unit to measure the concentration of particles exiting the unit. This allowed estimation of the number of particles deposited on the tip thereby allowing the calculation of the particulate mass deposited on the tip as described later.

A high voltage pulse generator (Vtech Engineering Inc., Andover, MA), specifically designed for spark spectroscopy, was used to create controlled and repeatable spark discharges in the electrode gap. A summary of the experimental parameters for the spark system is given in Table 2. A high voltage pulse generator, with output pulse energy (nominal) in the range of 50–300 mJ per pulse, was used to generate the spark plasma. The resulting spark plasma ablated the particulate mass collected on the cathode, followed by vaporization, atomization, and atomic emission. The atomic emission signal was collected as a backscattered light using a pierced mirror and two condensing lenses (50 mm diameter, focal lengths of 50 mm and 75 mm respectively). The signal was then focused and transmitted through a fibre-optic cable connected to a broadband spectrometer (200–980 nm, 0.1 nm resolution; LIBS 2500 Plus; Ocean Optics Inc.; Dunedin, FL). The triggering and timing of the high voltage pulse generator and the spectrometer was controlled by a digital delay generator. The compact broadband spectrometer allowed simultaneous analysis of multiple elements in the wavelength range of 200–980 nm.

Table 2 Experimental parameters of spark generation system

Spark energy input	50–300 mJ per pulse
Spectrometer wavelength range	200–980 nm
Integration time	1 ms
Aerosol sample flow rate	1.5 l min^{-1}
Operating voltage for corona	3 kV
Distance between the needles	5–6 mm
Diameter of cathode	500 μm
Diameter of anode	200 μm with 5 μm sharp tip

Calibration procedure

The calibration procedure for this system was described in detail elsewhere.[9] We employed the same procedure in this work and it is only briefly described below. The procedure consists of: (i) generation of test aerosols, (ii) collection of a predetermined amount of particulate mass on the electrode tip, (iii) application of the high voltage pulse to create the spark plasma, (iv) recording of the atomic emission signal using predetermined delay time, (v) calculation of the peak-to-base ratio for a desired element, and (vi) construction of the calibration curve by repeating the above process for different particulate mass on the electrode.

Calibration aerosols for desired elements were generated by nebulization of elemental standard solutions (for Si, Cr, Pb) and a known salt solution (for Na). The aerosol was collected on the collection electrode (or cathode) for a fixed amount of time followed by the spark discharge. The particulate mass of an element deposited on the electrode was estimated by using the collection time, aerosol flow rate, inlet particle number concentration, particle capture efficiency, chemical composition, and the density of the salt in the standard solution. Particle capture efficiency ($\eta(d_p)$) was estimated by measuring the particle number concentration downstream of the collection unit using a CPC, with (N_{out}^{HV}) and without ($N_{out}^{V=0}$) the presence of the electric field across the electrodes.

$$\eta(d_p) = \frac{N_{out}^{V=0}(d_p) - N_{out}^{HV}(d_p)}{N_{out}^{V=0}(d_p)} \quad (1)$$

The collection or capture efficiency thus defined incorporated all the particle losses including the wall loss and diffusion loss in the absence of electric field between the electrodes. In this study, 150 nm particles were used to generate the calibration curve. The collection efficiency for this particle size was about 90%. The collection efficiency was measured for every single experiment, and was used to calculate the total mass deposited on the electrode.

The atomic emission from the analyte was collected using the spectrometer and analysed. The peak to base (P/B) ratio of a chosen analyte atomic emission line was calculated, which was defined as the integrated absolute atomic emission line intensity normalized to the plasma continuum intensity close to the atomic line spectral region. The mass loading was varied by varying the collection time and for each mass loading, five different sets of measurements were performed. For each element, the calibration curve was constructed by plotting the P/B ratio as a function of mass deposited on the collection electrode tip. For determination of the limit of detection (LOD), a fixed delay time of 30 μs and spark energy of 150 mJ per pulse (nominal) was used for all the elements. An optimum 30 μs delay was chosen after studying the evolution of spectral response of analyte using Na aerosol at 150 mJ per pulse. The LOD was estimated using 3-σ criteria defined by the International Union of Pure and Applied Chemistry[29] as,

$$LOD = 3\sigma/S, \quad (2)$$

where σ is the standard deviation of the blank at the spectral region for each element and S is given by the slope of the calibration curve.

Experimental characterization of the plasma

To estimate the temperature of the pulsed spark plasma, the Boltzmann plot method was used. Lutetium (Lu) aerosol was generated as described earlier and was deposited on the cathode over a collection time of one minute. Lu lines at 325.43, 347.25, 350.74 and 355.44 nm were used for calculating the excitation temperature using the Boltzmann plot. Lu was chosen as multiple strong lines were observed within a narrow spectral window (339.71–355.44 nm). The relevant spectral lines and the spectroscopic data are listed in Table 3. Key assumptions involved for measuring temperature using this method were met, which included: (i) well separated upper energy levels of the lines used in the calculations, and (ii) high spectral intensity of the lines. The excitation temperature was deduced from the slope of the Boltzmann plot.

Electron density in the spark plasma was estimated by measuring Stark broadening of H_α lines (82 259.2865–102 823.911 cm^{-1}). Of various broadening mechanisms (*i.e.* Stark, Doppler, van der Waals, and Holtsmark resonance broadening), the Stark effect is typically the main contributor to line broadening in laser-induced or spark plasmas, especially during early times.[30] The Doppler width depends on the absolute temperature of the gas and atomic mass of the species and has been listed for the H_α line. For a temperature of 11 000 K, Doppler full width at half maximum (FWHM) is estimated to be 0.047 nm for the H_α line which is smaller than the spectral resolution of the spectrometer used in this study. Therefore, it can be neglected. In the present study, instrument broadening was measured using a mercury–argon lamp source (HG-1, Ocean Optics) and a Lorentzian profile was fitted to the instrument profile to obtain FWHM, $\Delta\lambda_{instrument}$. FWHM of the H_α line, $\Delta\lambda_{measured}$, was also obtained by fitting a Lorentzian profile to the observed H_α line. The Stark width of the H_α line, $\Delta\lambda$, was obtained by the linear subtraction of FWHM of observed profile to that of the instrument profile.[30] For the H_α line, the simplified form of the expression for electron number density can be represented as

$$n_e = 8.02 \times 10^{12}(\Delta\lambda/\alpha)^{3/2}\ cm^{-3} \quad (3)$$

where $\Delta\lambda$ is in Å and α is the half width of the reduced stark profiles in Å. α is a weak function of the electron density and temperature as tabulated in Griem's table.[31,32]

Results and discussions

Spark plasma evolution and dynamics

Fig. 3 shows typical spectra obtained from the spark discharge at two different delay times of 10 and 25 μs. The *y*-axis of the 10 μs spectra has been displaced upward by 1000 counts for clarity. As mentioned earlier, all measurements have been performed using a fixed, 1 ms integration time of the spectrometer, while the gate delay was varied. Comparison of 10 and 25 μs spectra shown in Fig. 3 clearly indicates that: (i) the continuum emissions considerably decay with time, (ii) most ionic lines also quickly decay with time, and (iii) neutral W lines, sampled from the cathode, are present at both early and later times. These observations, which are linked to the evolution of the spark plasma, are consistent with earlier observations regarding spark formation and evolution.[12,14,15,17,33] As Walters *et al.* noted, spark formation in air takes place in two steps: (i) a high voltage (HV) pulse on the order of few kV is applied to form a conducting ion channel between the electrodes to induce dielectric breakdown of air; this typically occurs in the first few nanoseconds of the application of the HV pulse;[17,34] and (ii) once the ion channel is established, a finite amount of energy is deposited in the inter-electrode gap, leading to a controlled spark discharge.

The key steps in the evolution of the spark plasma are shown in Fig. 4. The moving ion channel established in step one above is directed towards the cathode which mainly consists of the excited ions from the gas in the inter-electrode space.[12,16,17] This is consistent with our observation of ionic spectra at early delay times in Fig. 3. Subsequently, in step two, the ion channel further spatially expands due to energy deposition, at which point the plasma can be described using two overlapping regions (i)

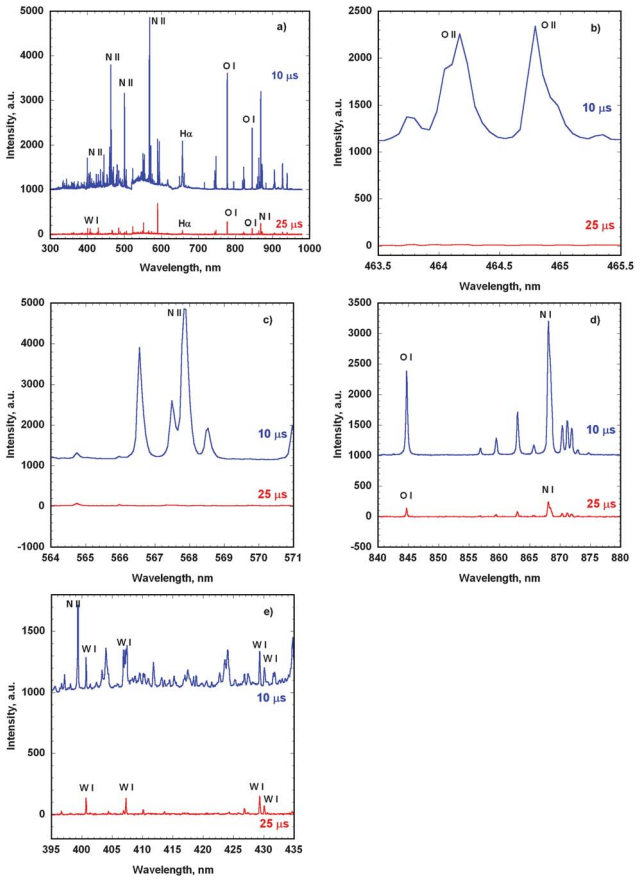

Fig. 3 (a–e) Plasma emission at two different time delays (10 and 25 μs). (b–e) Magnified spectra of different regions.

Table 3 Lu II spectroscopic data[46]

Wavelength, nm	Energy, cm^{-1}	Ag, s^{-1}
339.71	11 796–41 224.96	3.5×10^8
347.25	12 435–41 224.96	4.2×10^8
350.74	0–28 503	0.2×10^8
355.44	17 332–45 458	14.0×10^8

a central conducting channel (evolved from the moving ion channel), and (ii) a plasma plume at the cathode surface which is rapidly expanding radially due to space–charge effects as shown in Fig. 4.[17,20] These two regions differ in terms of the abundance of different species. The central channel consists mostly of highly energetic ionic species from the ambient gas as well as some from the vapour sampled from the cathode.[24,35] In contrast, the evolving plasma plume at the cathode surface mainly consists of neutral atoms from the cathode vapour in the exterior region and energetic ionic and neutral species (of the cathode vapour) in the interior core. As the energy deposition in the inter-electrode gap further ceases, the central conducting channel rapidly shrinks while the plasma plume still continues to expand due to thermal effects. Eventually, the plasma spatially grows to be more homogeneous once the energy deposition ceases.[36] The optical emission during this phase is dominated by the atomic emission from the neutral atoms while the continuum is negligible as evident in Fig. 3(a)–(e).

To further probe the temporal variation of spectral signals, integrated intensities of N II, N I, W I (from cathode), and Na I (from particles deposited on the cathode) were tracked as a function of the delay time. Absolute intensities were calculated by subtracting the base from the raw spectrum and then integrating the subtracted peak. With increase in delay time, decrease in line intensity is observed for all three species. The source of the ionic nitrogen line is mainly from the central conducting channel during the energy deposition process as noted above. It has been shown that for spark discharges in air, the evolution of the line intensity of N II closely follows the evolution of the current in the conducting channel.[15] Therefore, from the evolution of N II signal in Fig. 5, it can be concluded that the energy deposition ceases after 15–20 μs, which further leads to the disappearance of the central conducting channel and the ionic species therein. The N I signal persists for a longer duration compared to N II, as the decay of N II supplements the concentration of N I species, even after the conducting channel ceases to exist. By 25–30 μs, the emission from the N I species present in the conducting channel disappears completely. The plasma is relatively more homogenized by this delay time and consists mostly of neutral W I species from the cathode vapor. Fig. 4 also shows that the intensity of the neutral tungsten line slightly increases at about 15 μs, which is when the central conducting channel disappears. The rise in W I intensity could be due to the increased collisional excitation of the neutral tungsten atoms by energetic ionic N and O species

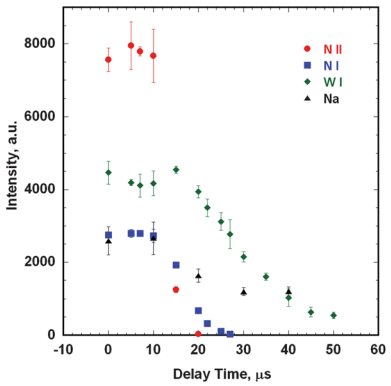

Fig. 5 Evolution of N II, N I, W I species as a function of time.

released from the conducting channel. As the plasma cools down further, the intensity of W I decreases monotonically. It is also worth noting that evolution of the Na I analyte signal is similar to that of tungsten, though the signal seems to decay at a much slower rate. Fig. 5 indicates that the emissions from the cathodic material and the analyte (on the cathode surface) persist for a longer time than the emissions from the ambient species present in the central conducting channel. The figure also shows that measurement of analyte signal after a time delay of 20–25 μs can yield improved signal-to-noise ratio.

Influence of spark energy on the spectral response

Fig. 6(a) shows the peak-to-base (P/B) variation of the W I line as a function of delay time for various levels of energy of the spark discharge. For lower energy, the maximum occurs earlier and is lower in value compared to that at higher energy. As the nominal spark energy increases, it leads to: (i) increased sampling from the cathode, (ii) higher temperatures and electron densities in the conducting channel, and thereby (iii) increase in concentration of energetic species in the conducting channel. The diameter of the central spark channel also grows with increasing spark discharge energy. Overall this results in increased collisional excitation of the cathode vapour in the plasma leading to higher P/B values with higher energy. At extremely high energies, both the line intensity as well as the background emissions are enhanced, thereby offsetting the advantages offered by higher energy and any improvements in P/B. It is also observed in Fig. 6(a) that the signal persists for a longer time at higher energies. Similar characteristics

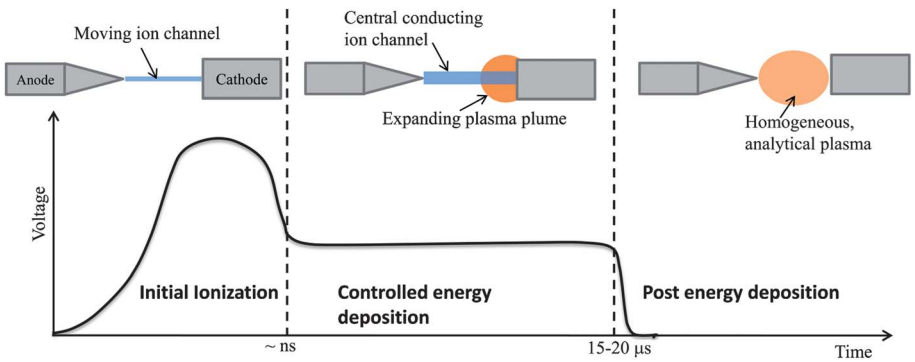

Fig. 4 Growth of the spark plasma during and after energy deposition.

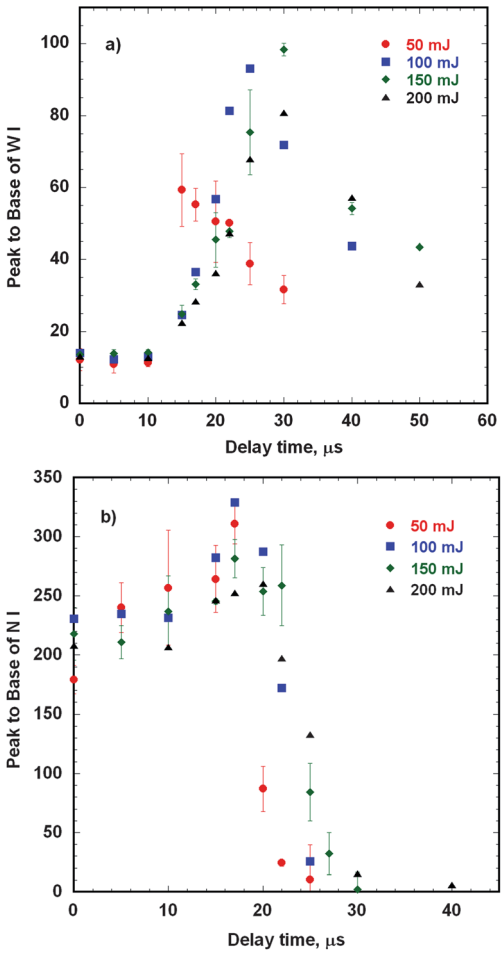

Fig. 6 P/B of (a) W I, (b) N I as a function of time and spark energy.

are observed for the N I line in Fig. 6(b) but the decay is much faster. Based on these data, a nominal energy level of 150 mJ per pulse was used for subsequent calibration in this work.

Plasma temperature and electron density

Fig. 7 shows the temporal evolution of spark plasma temperature using Lu emission lines as discussed earlier. It should be noted

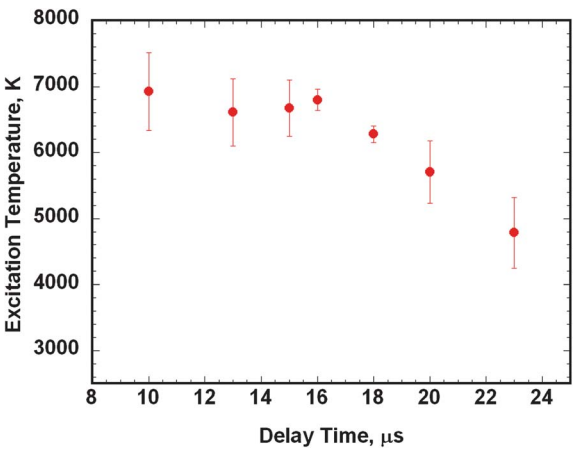

Fig. 7 Temporal evolution of the excitation temperature.

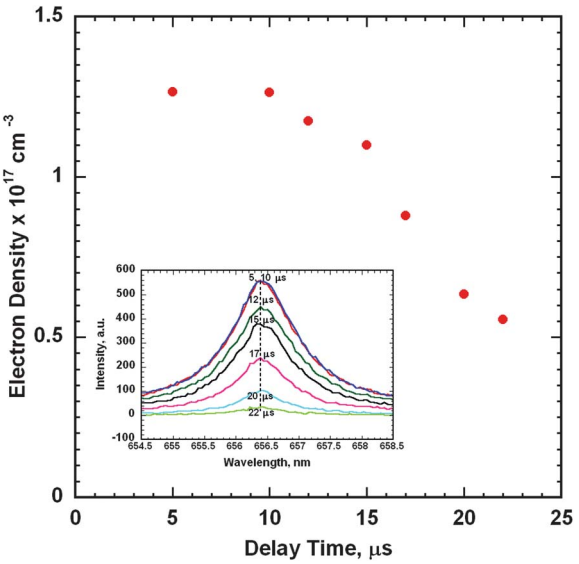

Fig. 8 Temporal evolution of electron density. Inset image shows the profile of the stark broadened H_α line.

that this temperature is the time-averaged analyte excitation temperature (over $t_i - t_d$; where t_i is the total integration time of 1 ms, and t_d is the delay time). During early times in the plasma, when the conduction channel is present, the average temperature is in the range 6500–7000 K which is slightly lower, but comparable to temperatures attained in laser-induced plasmas using similar energy input.[37–39] After the central conducting channel ceases (at about 15–20 μs), the temperature starts decreasing rapidly due to thermal expansion of the plasma, and reaches ~4500 K by 23 μs.

A similar trend in the electron density is observed as a function of delay time as shown in Fig. 8. Also shown in the inset, are the intensity profiles of the H_α line at various delay times ranging from 5 to 22 μs. The electron density was 1.2×10^{17} cm^{-3} at 5–10 μs delay time and then decayed to 5×10^{16} cm^{-3} at 23 μs. Electron densities lower than ~10^{16} cm^{-3}, using the H_α line, can lead to overestimation of n_e as ion dynamics effects must be accounted for.[40] Electron density estimates in this study were above 10^{16} cm^{-3}; therefore ion dynamic effects can be neglected. During early times in the plasma, the central conducting channel contributes the majority of the electrons. The electron density change is negligible between 5 and 10 μs, after which it starts decreasing gradually till about 15 μs. There is a rapid decrease in electron density after 15 μs which coincides with the time when the conducting channel ceases to exist.

Reproducibility of the plasma characteristics

The repeated spark generation can lead to changes in the morphology of the cathode and anode surfaces, raising questions about repeatability of plasma characteristics and the resulting optical signal. We investigated repeatability of W I (from cathode) and N I (from ambient air) signals as a function of the number of sparks to probe this issue. Fig. 9 shows variation in N I and W I signals as a function of the number of spark discharges. A continuous train of pulsed spark discharges were produced at 5 Hz and the optical signals (P/B ratio) of N I and

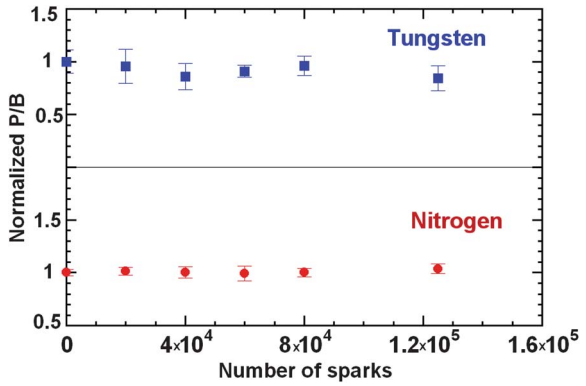

Fig. 9 Variation of P/B of N and W as a function of number of sparks.

W I were recorded (averaged over 5 replicates) every 20 000 spark discharges. The P/B signal for both species were normalized by their respective values at time $t = 0$. As evident in Fig. 8, no systematic drift was observed for W I and N I signals even after 125 000 sparks. The variation in P/B signals (as a function of the number of sparks) of W I was within 3–7% and that for N I was 6–17%. This variation is of the same order as the uncertainty in each data point which ranged from 2% to 15%. We measured the response of the deposited analyte (Na) from the fresh electrode and from the electrode after thousands of sparks and no significant change in the analyte response was observed.

Particle collection and ablation

Calibration of our system requires that the amount of particulate mass deposited on the collection electrode is known with good precision and accuracy. Therefore, the collection efficiency must remain constant during the entire duration of particle deposition. Particle collection efficiency of our system was 90% for the entire range of collection times (5 seconds to 20 minutes) used in the calibration experiments. This implied that the collection efficiency did not vary as a function of the accumulated particle mass on the collection electrode. A detailed discussion about collection efficiency and the factors affecting it are presented elsewhere.[9] Here, our focus was only to ensure consistency, accuracy, and precision of measurements in the calibration process. Collection efficiency close to 99% can be achieved for particles in the size range of 30–600 nm by employing either a one-step charge-and-collect scheme or two-step charging, followed by collection scheme.[9]

Another key requirement, with respect to reliable calibration, is that the fraction of the total particulate mass that gets ablated by the spark plasma must be constant (or ideally 100%) and does not vary from one spark event to the other. We believe that the sampling of particulate mass (on cathode) by the plasma occurs *via* the same mechanisms responsible for sampling of cathodic material itself. The energetic ions (from the gas in the inter-electrode gap), produced at early times during the formation of the moving ion channels, strike the cathode surface with high energy leading to vaporization and atomization of the deposited particulate mass (*i.e.* analyte) as well as the cathode itself. The ejected atoms from the analyte and the cathode rapidly move away from the cathode due to space–charge effects, and undergo excitation by various mechanisms including charge transfer;[20] these atoms further migrate into the inter-electrode gap.[24,36]

Sampling of the cathode as well as the deposited particles on the cathode surface is dependent on the amount of charge passed to the cathode during current conduction phase.[17] A majority of the sampling from the cathode surface takes place during this current conduction phase. The sampling process is spatially localized (on the order of few hundred micrometres); however the spatial wandering of the cathode space charge can affect sampling.[17] In our system, the cathode diameter is 500 μm, and a relatively large current conduction phase is employed (~15 to 20 μs). This leads us to believe that perhaps most of the particulate mass deposited on the cathode surface is sampled. Further, Walters and co-workers have also shown that spark plasmas in nitrogen rich environments can promote wandering of the plasma plume on the cathode surface, thereby allowing sampling of a larger portion of the cathode surface.[17] Our experiments were conducted in air, implying the possibility of efficient sampling of the entire cathode surface (and hence the particulate mass thereupon). No experiments were conducted to further probe the mechanisms affecting particle sampling, and will be a subject of future studies. However, as will be shown later, we observed excellent repeatability of signal (<15%) for all analytes used in this study, implying that the fraction of particulate mass ablated—though unknown—is constant across all particle types.

Calibration and limit of detection

For each element, the calibration curve was constructed by plotting the P/B ratio as a function of mass deposited on the collection electrode tip. The amount of particles deposited on the tip was controlled by changing the collection time which ranged from 5 seconds to 20 minutes. The mass deposited on the electrode tip is based on the actual measured collection efficiency for each particle type used in this study and implicitly accounts for particle shape and relative humidity of aerosol used in our experiments.

Five sets of measurements were performed for each mass loading. For lower mass loading, a single spark was sufficient to

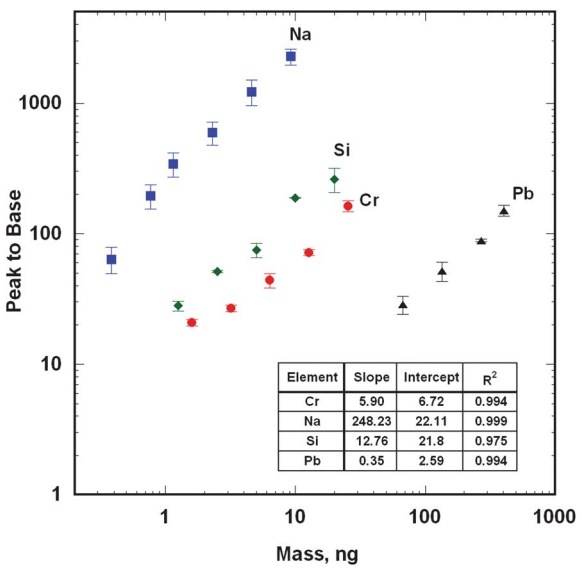

Fig. 10 Calibration curves for Na, Cr, Pb and Si.

Table 4 Comparison of detection limits in terms of mass and air concentration for various elements[a]

	Limit of detection (this work)			
Element	Mass, pg	Air concentration, ng m^{-3}	% RSD range	LOD (references)
Cr (520.84 nm)	11	0.44	5–12	35 pg, 0.047 μg m^{-3} (Diwakar *et al.* 2012 (ref. 9))[b] 0.17 pg (Lithgow *et al.* 2004 (ref. 44))[b] 0.11 μg m^{-3} (Panne *et al.*, 2001 (ref. 47))[b] 10 μg m^{-3} (Hunter *et al.* 2000 (ref. 27))[c]
Na (589.99 nm)	28	1.13	6–13	18 pg, 0.02 μg m^{-3} (Diwakar *et al.* 2012 (ref. 9))[b] 0.0033 pg (Carranza *et al.*, 2001 (ref. 48))[b] 2 μg m^{-3} (Amodeo *et al.* 2009 (ref. 42))[b] 190 pg (McDonald *et al.* 1989 (ref. 24))[c]
Pb (405.78 nm)	1750	70	3–15	155 μg m^{-3} (Neuhauser *et al.* 1997 (ref. 49))[b] 10 μg m^{-3} (Hunter *et al.* 2000 (ref. 27))[c]
Si (568.88 nm)	800	32	2–11	20 μg per dscm (Buckley *et al.* 2000 (ref. 50))[b]

[a] Air concentration calculated at flow rate of 5 l min^{-1} and collection time of 5 minutes. [b] Laser-induced breakdown spectroscopy. [c] Spark emission spectroscopy.

ablate all the analyte material deposited on the cathode, while for higher mass loading multiple sparks were required. For the multiple spark case, P/B of a specific analyte from all spark events was summed to obtain the total spectral response as described elsewhere.[9] Representative calibration curves for Cr, Na, Pb, and Si, are shown in Fig. 10. The data point on each calibration curve represents the average over five replicates. The error bar on each data point represents standard deviation around the mean. All calibration curves in this study were described using a linear curve over a mass range spanning at least one order of magnitude. Table 4 lists the mass detection limits of various elements studied in this work, which ranges from 11 to 800 pg. Reported LOD values are within a factor of 10 of the smallest measured mass, except for Cr and Pb, in the calibration experiments, following conventional practice in plasma spectroscopy.[41] Detection limits in terms of the air concentration in the range of 0.44–70 ng m^{-3} were obtained by assuming a flow rate of 5 l min^{-1} and a collection time of 5 minutes. Table 4 also shows the range of % relative standard deviation (based on the error bars in Fig. 10) of each analyte, which indicates the repeatability or reproducibility of a spectral response. The reproducibility ranged from 2 to 15% for the analytes studied in this work.

Also shown in Table 4, for comparison, are LOD values from other LIBS and spark plasma studies on aerosols. As evident from this comparison, LODs in terms of air concentration are significantly better than those obtained in other laser-induced or spark plasma studies. Detection limits in our system can be further improved by employing gated detectors such as the integrated charge coupled device (ICCD). The relative standard deviation (RSD) at various mass loadings was in the range of 2–15% which is much better compared to LIBS or spark plasma systems employing free stream approach for aerosol analysis.[42–44] Higher RSDs, typically in the range of 10–20%, have been reported for filter-based LIBS analyses.[45] The repeatability of measurements is also better than that obtained using laser-induced plasma in our earlier study.[9]

Conclusions

An aerosol preconcentration method has been effectively coupled with spark emission spectroscopy to allow near real-time measurement at low limits of detection. For elements studied in this work (Na, Cr, Si, Pb), detection limits in the range of 0.44–70 ng m^{-3} can be obtained at a time resolution of 5 minutes at a flow rate of 5 lpm. Similar detection limits are expected for other elements. The reproducibility of spectral response was excellent and ranged from 2 to 15%. The overall figures of merit of the approach are superior to other microplasma based techniques for aerosol analysis. This preliminary work clearly demonstrates the key advantages offered by our approach: (i) ability to perform relatively accurate and precise calibration of the system compared to other existing aerosol sampling or collection techniques, (ii) potential for low detection limits and sensitivity, and most importantly, (iii) near-real time measurement capability. The simplicity and robustness of the technique are particularly appealing for implementation in field-portable aerosol instrumentation.

Acknowledgements

The authors would like to thank Patrick Cobler of Vtech Engineering Corp. for generously loaning the high voltage pulse generator for this study. The authors are also thankful to Dr J.P. Walters for fruitful discussions on fundamentals of spark emission spectroscopy. Careful review and comments of reviewers are also gratefully acknowledged.

Notes and references

1 H. J. Gibb, P. S. J. Lees, P. F. Pinsky and B. C. Rooney, *Am. J. Ind. Med.*, 2000, **38**, 115–126.
2 K. Donaldson, L. Tran, L. A. Jimenez, R. Duffin, D. E. Newby, N. Mills, W. MacNee and V. Stone, *Part. Fibre Toxicol.*, 2005, **2**, 1.
3 E. P. Agency, *Fed. Regist.*, 2011, 24976–25147.
4 NTP, in *National Toxicology Program*, ed. U. S. Department of Health and Human Services, 2011, p. 499.
5 OSHA, http://www.osha.gov/SLTC/metalsheavy/index.html, 2011.
6 U. Code, 2008, pp. 5673–5695.
7 G. Oberdorster, V. Stone and K. Donaldson, *Nanotoxicology*, 2007, **1**, 2–25.
8 *2008 Direct-Reading Exposure Assessment Methods (D.R.E.A.M.) Workshop*, NIOSH, ed. U. S. D H H S, 2009.
9 P. Diwakar, P. Kulkarni and M. E. Birch, *Aerosol Sci. Technol.*, 2012, **46**, 316–332.
10 J. Joly, *Proc. R. Soc. London*, 1889, **47**, 67–85.
11 J. P. Walters, *Appl. Spectrosc.*, 1969, **23**, 317.

12 J. P. Walters, *Science*, 1977, **198**, 787–797.
13 J. P. Walters, *Appl. Spectrosc.*, 1968, **22**, 364.
14 J. P. Walters, *Appl. Spectrosc.*, 1968, **22**, 366.
15 R. D. Sacks and J. P. Walters, *Anal. Chem.*, 1970, **42**, 61.
16 J. P. Walters, *Appl. Spectrosc.*, 1972, **26**, 17.
17 J. P. Walters, *Appl. Spectrosc.*, 1972, **26**, 323.
18 R. J. Klueppel and J. P. Walters, *Spectrochim. Acta, Part B*, 1980, **35**, 431–446.
19 J. P. Walters and W. S. Eaton, *Anal. Chem.*, 1983, **55**, 57–64.
20 J. P. Walters and S. A. Goldstein, *Spectrochim. Acta, Part B*, 1984, **39**, 693–728.
21 D. J. C. Helmer and J. P. Walters, *Appl. Spectrosc.*, 1984, **38**, 392–398.
22 D. J. C. Helmer and J. P. Walters, *Appl. Spectrosc.*, 1984, **38**, 399–405.
23 J. C. Williams, J. E. Kuehn, J. T. Coleman and T. A. Mausert, *Anal. Chem.*, 1984, **56**, 2735–2740.
24 J. T. Mcdonald, J. C. Williams and J. C. Williams, *Appl. Spectrosc.*, 1989, **43**, 697–702.
25 M. Resano, E. Garcia-Ruiz, K. S. McIntosh, J. Hinrichs, I. Deconinck and F. Vanhaecke, *J. Anal. At. Spectrom.*, 2006, **21**, 899–909.
26 J. Wienold, H. Traub, B. Lange, T. Giray, S. Recknagel, H. Kipphardt, R. Matschat and U. Panne, *J. Anal. At. Spectrom.*, 2009, **24**, 1570–1574.
27 A. J. R. Hunter, J. R. Morency, C. L. Senior, S. J. Davis and M. E. Fraser, *J. Air Waste Manage. Assoc.*, 2000, **50**, 111–117.
28 A. J. R. Hunter, S. J. Davis, L. G. Piper, K. W. Holtzclaw and M. E. Fraser, *Appl. Spectrosc.*, 2000, **54**, 575–582.
29 P. W. J. M. Boumans, *Anal. Chem.*, 1994, **66**, A459–A467.
30 D. W. Hahn and N. Omenetto, *Appl. Spectrosc.*, 2010, **64**, 335a–366a.
31 H. R. Griem, *Spectral Line Broadening by Plasmas*, Academic Press, New York, 1974.
32 H. R. Griem, *Plasma Spectroscopy*, McGraw-Hill, New York, 1964.
33 A. Scheeline, *Prog. Anal. At. Spectrosc.*, 1984, **7**, 21–65.
34 P. Stritzke, I. Sander and H. Raether, *J. Phys. D: Appl. Phys.*, 1977, **10**, 2285–2300.
35 N. L. Aleksandrov and E. M. Bazelyan, *Plasma Sources Sci. Technol.*, 1999, **8**, 285–294.
36 M. Ramli and K. Wagatsuma, *ISIJ Int.*, 2010, **50**, 864–867.
37 P. K. Diwakar, S. Groh, K. Niemax and D. W. Hahn, *J. Anal. At. Spectrom.*, 2010, **25**, 1921–1930.
38 P. K. Diwakar, P. B. Jackson and D. W. Hahn, *Spectrochim. Acta, Part B*, 2007, **62**, 1466–1474.
39 O. A. Nassef and H. E. Elsayed-Ali, *Spectrochim. Acta, Part B*, 2005, **60**, 1564–1572.
40 C. Yubero, M. D. Calzada and M. C. Garcia, *J. Phys. Soc. Jpn.*, 2005, **74**, 2249–2254.
41 J. D. Ingley and S. R. Crouch, *Spectrochemical Analysis*, Prentice Hall Inc, Upper Saddle River, NJ, 1988.
42 T. Amodeo, C. Dutouquet, O. Le Bihan, M. Attoui and E. Frejafon, *Spectrochim. Acta, Part B*, 2009, **64**, 1141–1152.
43 M. D. Cheng, *Talanta*, 2003, 127–137.
44 G. A. Lithgow, A. L. Robinson and S. G. Buckley, *Atmos. Environ.*, 2004, **38**, 3319–3328.
45 F. Y. Yueh and J. P. Singh, *Laser-Induced Breakdown Spectroscopy*, Elsevier, 2007.
46 J. E. Sansonetti and W. C. Martin, *J. Phys. Chem. Ref. Data*, 2005, **34**, 1559–2259.
47 U. Panne, R. E. Neuhauser, M. Theisen, H. Fink and R. Niessner, *Spectrochim. Acta, Part B*, 2001, **56**, 839–850.
48 J. E. Carranza, B. T. Fisher, G. D. Yoder and D. W. Hahn, *Spectrochim. Acta, Part B*, 2001, **56**, 851–864.
49 R. E. Neuhauser, U. Panne, R. Niessner, G. Petrucci, P. Cavalli and N. Omenetto, *Sens. Actuators, B*, 1997, **39**, 344–348.
50 S. G. Buckley, H. A. Johnsen, K. R. Hencken and D. W. Hahn, *Waste Manag.*, 2000, **20**, 455–462.